Gravity waves in Jupiter's stratosphere, as measured by the Galileo ASI experiment

Leslie A. Young
Southwest Research Institute,1050 Walnut St Suite 400, Boulder CO 80302
Roger V. Yelle
Lunar and Planetary Lab, University of Arizona, 1629 E Univ. Blvd, Tucson AZ 85721
Richard Young, Alvin Seiff*
NASA Ames Research Center, MS 245-3, Moffett Field CA, 94035
Donn B. Kirk
37465 Riverside Dr, Pleasant Hill, OR 97455

*Deceased.

Submitted to Icarus *December 10, 2002*

40 manuscript pages, including 7 figures and 5 tables.

Running head: Gravity waves in Jupiter's stratosphere

Direct editorial correspondence to:

Leslie A. Young

Southwest Research Institute

1050 Walnut St. Suite 400

Boulder CO 80302

email: layoung@boulder.swri.edu

Phone: (303) 546-6057

FAX: (303) 546-9687

Abstract

The temperatures in Jupiter's stratosphere, as measured by the Galileo Atmosphere Structure Instrument (ASI), show fluctuations that have been interpreted as gravity waves. We present a detailed description of these fluctuations, showing that they are not likely to be due to either measurement error or isotropic turbulence. These fluctuations share features with gravity waves observed in the terrestrial middle atmosphere, including the shape and amplitude of the power spectrum of temperature with respect to vertical wavenumber. Under the gravity wave interpretation, we calculate ranges of energy deposition and heat fluxes, place limits on the eddy Prandtl number, and compare predicted and observed eddy diffusion coefficients. We find that wave heating or cooling is likely to be important in Jupiter's upper stratosphere, that the Prandtl number lies between 1 and 4.4, and that diffusive filtering theory is a poor predictor of the eddy diffusion coefficient in Jupiter's atmosphere.

Keywords: ATMOSPHERES, DYNAMICS; JUPITER, ATMOSPHERE;

1. Introduction

The Atmosphere Structure Instrument (ASI) on the Galileo probe measured densities and temperatures in Jupiter's stratosphere that vary on scales ranging from 50 km to the limit of the resolution (2-4 km/point). Temperature variations on scales less than a scale height have also been seen in stellar occultations (e.g., French and Gierasch 1974) and radio occultations (Lindel et al. 1981). Interpretations of these small-scale temperature variations include turbulence (Jokipii and Hubbard 1977), gravity waves (French and Gierasch 1974), or planetary-scale, longer-lived phenomena (Allison 1990, Friedson 1999). The characteristics of the temperature or density variations are the key to interpreting the data in terms of the underlying dynamics. The ASI data combines high vertical resolution with a large range of altitudes, permitting a more detailed examination of the statistics of Jupiter's stratosphere than previously possible. Stratospheric temperature and density fluctuations have also been reported in the middle atmospheres of Titan and the other giant planets (e.g., Cooray et al. 1998, Sicardy et al. 1985, Roques et al. 1994). The quantitative description of the thermal and density variations presented here will help with comparative planetology, by establishing whether temperature variations in the outer planets exhibit a "universal power spectrum," as temperatures appear to do in the Earth's middle atmosphere (VanZandt 1982).

We describe the ASI measurements and errors in Section 2. In Section 3, we present a statistical analysis of Jupiter's stratosphere, with interpretation. The results are discussed in Section 4, and our conclusions are summarized in Section 5.

2. Observations

The Galileo probe entered Jupiter's atmosphere at a latitude of 6.5° North in December 1995. The temperatures presented here (Fig 1) are based on the deceleration of the probe measured by two axial accelerometers on the Atmosphere Structure Instrument

(ASI) during the probe entry phase, before parachute deployment (Sieff et al. 1992; Seiff et al. 1998, hereafter S98). The measurements made by the ASI are presented in detail in S98. We expand on S98 here by including an analysis of the statistical errors in the densities and temperatures at the smallest scales.

In this paper, we concentrate on Jupiter's atmosphere between the troposphere (dominated by convection) and the thermosphere (dominated by conduction). This region is dominated by radiative processes, and corresponds to the stratosphere and mesosphere in the terrestrial atmosphere. Since Jupiter, unlike Earth, has no well-defined stratopause, this entire region is referred to as either the middle atmosphere or the stratosphere; the interface between this region and the thermosphere is usually referred to as the mesopause, again in analogy with terrestrial terminology. For the remainder of the paper, we will refer to this radiative region as the stratosphere. By this definition, Jupiter's stratosphere, as measured by the ASI profile, extends from the tropopause at 28 km (280 mbar) to the mesopause at ~350 km (~0.001 mbar). The altitudes in this paper are defined relative to the 1 bar level, and are identical to those from S98.

Insert Figure 1 (Temperatures derived by the Galileo ASI)

The ASI used two accelerometers, denoted z_1 and z_2. S98 determined that there was no systematic difference between the temperature profiles measured by the two accelerometers, and presented only the z_1 data. Because this paper is concerned with the statistics of temperature and density fluctuations at the smallest scales, we analyze data from both accelerometers. Additionally, eight data points in the stratosphere that appeared anomalous were smoothed for the profile presented in S98. However, these points do not deviate statistically from the mean temperature profile; two of the smoothed points are $\lesssim 2\ \sigma_T$ from the mean temperature, where σ_T is the standard deviation of the observed temperatures, and the remaining six points are $< 1\ \sigma_T$ from the mean. Similarly, none of the derivatives arising from the smoothed points are unusual. Finally, when the z_1

temperatures are overplotted with the z_2 data, the smoothed points no longer appear anomalous. We therefore reinstate all eight points. We include the stratospheric data used here in Tables I and II.

Insert Tables I and II (Stratospheric heights; temperatures; pressures; number density; acceleration; digitization error)

We limit our analysis to the region between 90 and 290 km, where the mean temperature (e.g., a vertically smoothed temperature) is essentially isothermal. This avoids the sharp gradients just above and below this isothermal zone, which would otherwise complicate the characterization of deviations of temperature from a background mean. The probe velocity within this range exceeded Mach 1 (S98), so buffeting of the probe contributed negligibly to the measured deceleration. The solid points in Fig. 1 indicate this 90-290 km range. Other characteristics of the ASI measurements through this range are summarized in Table III.

Insert Table 3 (ASI characteristics of the region considered here)

The basic measurement during the ASI entry phase is the deceleration of the probe. The error in the measured deceleration is dominated by the sensor resolution. As described in S98, each of the two accelerometers had four sensitivity ranges. The ASI accelerometers began their entry into the stratosphere in range 2, entered into range 3 from 284 to 211 km, and then finished in range 4 below 211 km. Within each sensitivity range the accelerometers have a constant sensor resolution (9.6×10^{-4}, 3.1×10^{-2}, and 0.98 m s^{-2} for ranges 2, 3, and 4 respectively). The fractional acceleration resolution, ε_a (accelerometer resolution divided by measured acceleration) is given in Tables I and II. Fig. 2 plots the normalized fluctuation in the deceleration ($\Delta a = (a - \bar{a})/\bar{a}$, where a is the measured acceleration and $\bar{a}$ is an estimate of the waveless acceleration), along with error bars with length $\varepsilon_a/2$.

Insert Figure 2 (Relative errors)

Since the probe's deceleration is the product of the atmospheric density and a slowly varying factor that includes the drag coefficient and the probe velocity (S98), $\Delta\rho \approx \Delta a$, where $\Delta\rho = (\rho - \overline{\rho})/\overline{\rho}$ is the normalized density fluctuations. Fig. 2 shows the close relation between $\Delta\rho$ and Δa. To a very good level of approximation, the fractional density resolution (ε_ρ) equals ε_a.

Assuming hydrostatic equilibrium, the pressure at the i^{th} point (p_i,) can be expressed as a sum involving observed densities at altitudes higher than the i^{th} point (for observations ordered in decending altitude, densities ρ_j, where $j \le i$). The temperature at the i^{th} point (p_i,) can then be calculated from the pressure and density assuming an ideal gas. Combining these into one equation expressing temperature as a function of densities above the point of interest, one can calculate how the errors in density propagate into the temperature errors. The fractional temperature resolution at the i^{th} point (ε_{T_i}) can be expressed in terms of the errors in the measured densities ($\sigma(\rho) \approx \varepsilon_\rho\, \rho$) as

$$\varepsilon_{T_i}^2 = \frac{1}{T_i \rho_i}\left\{\sum_{j=1}^{i-1}\left[T_j \frac{d_j}{H_j}\sigma(\rho_j)\right]^2 + \left[T_i \sigma(\rho_i)\right]^2\right\}$$
$$d_j = \begin{cases} (z_0 - z_1)/2, & j = 0 \\ (z_{j-1} - z_{j+1})/2, & 0 < j < i \\ (z_{i-1} - z_i)/2, & j = i \end{cases} \qquad (1)$$

where z_j is the altitude, T_j is the temperature, H_j is the pressure scale height, and ρ_j is the density of the j^{th} point. The error in the temperature and density of the first datum contributes negligibly to the error in the stratospheric temperature. For errors in the thermal gradient, we note that $d\Delta\rho/dz = -d\Delta T/dz + \Delta T/H$, given hydrostatic equilibrium for an ideal gas. In our dataset, the $\Delta T/H << d\Delta T/dz$, and $d\Delta T/dz \approx d\Delta\rho/dz$ (Fig. 2). Thus, for calculating the error in temperature gradients, it is sufficient to assume $\varepsilon_T = \varepsilon_\rho$. Calculating the formal error in T using Eq. (1) increases ε_T by an average of only 10%. We therefore take $\varepsilon_T = \varepsilon_\rho$ throughout.

3. Analysis and interpretation

3.1 Overview of Jupiter's stratospheric temperature variations

Table IV summarizes some of the characteristics of this region of Jupiter's atmosphere, using the normalized temperatures and measurement resolutions from Tables I and II. We begin with a qualitative description of the stratosphere. A quantitative treatment follows in the remainder of this section.

The normalized temperature fluctuations for both accelerometers are shown in Fig. 3. Around Jupiter's essentially isothermal mean thermal profile between 90 and 290 km, the root-mean-square (rms) of the temperature fluctuations (σ_T) is 5.0 K. This is much larger than the fluctuation that would arise solely from the ASI digitization error. If the temperature fluctuations were due entirely to the measurement error, the rms variation would only be 0.2 K.

Insert Figure 3 (normalized temperatures)

Jupiter's stratosphere is not dominated by any single, quasi-monochromatic wave. There appear to be several wavetrains one or two cycles long, with the largest of these at 90-180 km, but also at 170-210 km (~10 km wavelength) and at 230-280 km (~20 km wavelength). However, the overall impression is of a complex collection of variations at a large range of scales, from several km to 60 km, with the larger temperature variations being at larger spatial scales.

Insert Table 4 (Mean T; altitude, number density, and pressure range; rms (ΔT); power spectra info; derivative info)

Qualitatively, the ASI temperature profile is similar to thermal profiles derived from radio or stellar occultations. In particular, Voyager radio occultations (Lindel et al. 1981) showed large temperature excursions at the base of Jupiter's stratosphere, and ground-based stellar occultations (e.g., French and Gierasch 1974) showed multi-scale fluctuations with small vertical scales in Jupiter's upper stratosphere.

3.2 Temperatures Derivatives

Fig. 4 shows vertical thermal gradients in Jupiter's atmosphere, calculated under the assumption that the temperature deviations are mainly attributable to derivatives with respect to height, rather than latitude, longitude, or time. This assumption is discussed further at the end of this section. Because the probe's velocity (Table III) is much larger then the expected velocities in Jupiter's stratosphere, we ignore changes in temperature along the probe's path caused by inhomogeneities advected by a mean wind. The gradients were derived individually for each of the two accelerometers to avoid artifacts that might be introduced by small differences in temperature or altitude scales. Fig. 4 shows that the gradients thus calculated are bounded on the negative side by the adiabatic lapse rate, as expected, and slightly exceed the negative of the adiabatic lapse rate on the positive side.

Insert Figure 4 (derivatives)

The plot of gradient vs. altitude shows a slightly skewed or scalloped character (e.g., rounded at the local minima, pointed at the local maxima), similar to that of gradients derived from stellar occultations of Titan's middle atmosphere (Sicardy et al. 1999). The skewness of the thermal gradients is seen graphically in their histogram (Fig. 5a, solid line). (Skewness measures the asymmetry of a distribution, and is defined by $\sum\left[\left(x_j - \bar{x}\right)/\sigma\right]^3 / N$, where $\bar{x}$ is the mean and σ is the standard deviation; Press et al., 1992) We tested the robustness of the histogram in two independent ways. First, we performed a Monte-Carlo analysis by generating 6400 sample temperature profiles, each differing from the measured profile by a uniform random distribution with a full-width equal to the derived digitization error, described in Section 2. The envelope of the histograms, shown as gray boxes in Fig. 5a, shows a similarly skewed distribution. Second, since the two accelerometers present us with two independent measurements of the same portion of Jupiter's stratosphere, we calculated the histograms of the gradients from each accelerometer independently (Fig. 5b,c). In all three histograms, the adiabatic

lapse rate and its negative are indicated, showing again that the negative derivatives are bounded by the lapse rate. The skewness of the distribution is listed in Table IV, where the error is calculated by the difference between the skewness of the combined *z1* and *z2* derivatives, and the skewness of each accelerometer independently. This skewness, 0.42±0.25, is only 1.7 σ significant. According to Press et al. (1992), roughly 750 measurements of the thermal gradient per profile (~250 m resolution) would be needed for a statically significant (> 3σ) measurement of the skewness.

Insert Figure 5 (derivative histogram)

Skewed distributions of thermal gradients have also been seen in the middle atmospheres of Titan (Sicardy et al 1999) and the Earth (Lui et al. 2001). On these bodies, as on Jupiter, the negative gradients are essentially bounded by the adiabatic lapse rate, with unbounded positive gradients. The skewness and the boundedness of the gradients suggest that the temperature fluctuations are limited by the onset of convective instability near the altitudes of maximum negative gradient (e.g., Chao and Schoeberl 1983; Fritts and Dunkerton 1985; Walterscheid and Schubert 1990), rather than by damping that operates throughout a fluctuation's wavelength (e.g., Lindzen 1981; Smith et al. 1987). As discussed in Section 4.3, this distinction has serious implications for the energetics of Jupiter's stratosphere.

The observed cut-off at the adiabatic lapse rate is physically meaningful and has analogies in observations of other middle atmospheres, supporting the conclusions of Section 3.1 that observed temperature and density fluctuations are not dominated by measurement error. Also, vertical variations dominate over temporal variations only if $(dT/dt) << (dT/dz)(v_z)$, implying $(dT/dt) << 5$ K/s, so periods range from $P >> 0.5$ s for 3 km waves and $P >> 3.5$ s for 20 km waves. Similarly, because the probe's horizontal velocity (v_x) is much larger than its vertical velocity (v_z), we conclude that the temperature and density fluctuations are highly stratified. The observed temperature and

density variations can only be dominated by the vertical derivatives present in the atmosphere at the time of entry if $(dT/dx) << (dT/dz)(v_z/v_x)$, so that horizontal derivatives are less than 0.3 K/km, and the observed structures have aspect ratios (ratios of horizontal to vertical scales) of > 8. It seems highly unlikely that the horizontal gradients or temporal variations would be just such as to give an apparent minimum thermal gradient near the adiabatic lapse rate by chance. We conclude that the observed variations are dominated by vertical gradients.

The derived aspect ratio (>8) is consistent with aspect ratios > 60 on Uranus (French et al. 1982), 25-100 on Neptune (Narayan & Hubbard 1988), and ~140 on Titan (Sicardy et al. 1999) from stellar occultations observed at multiple sites. Similarly, Narayan & Hubbard (1988) discuss evidence of large aspect ratios in the terrestrial upper atmosphere as well. Because the aspect ratio is much greater than one, we conclude that the observed fluctuations are not due to isotropic turbulence.

3.3 Identification of prominent wave-like structures

As mentioned previously, there are several prominent wave-like structures in the Galileo ASI data of roughly two wavelengths long. These are evident in the temperature profiles, and are even more distinct in the thermal gradient profiles. To quantify these apparent wavetrains, we fit portions of the data to the sum of a linear or quadratic background and a sine wave with an amplitude that is allowed to vary exponentially with altitude. Such a sine wave is consistent with gravity waves that are undamped, critically damped, or overdamped by eddy viscosity in an atmosphere with no vertical shear of horizontal wind. In terms of $\zeta = z - z_0$, the fitted functions are:

$$T = b + d\zeta + q\zeta^2 + ae^{-\alpha\zeta}\sin(m\zeta) \quad (2a)$$

$$dT/dz = d + 2q\zeta + ae^{-\alpha\zeta}\left[-\alpha\sin(m\zeta) + m\cos(m\zeta)\right] \quad (2b)$$

where m is the vertical wavenumber, a is the amplitude at z_0, $1/\alpha$ is the amplitude damping length, and b, d, and q are the terms of a quadratic background temperature. We

simultaneously fit Eq. 2a to the temperature profile and 2b to the derivative profile. The resulting wavetrains are tabulated in Table V and plotted in Figure 6.

Insert Figure 6 (wavetrain) and Table 5 (wavetrain)

Despite its large amplitude, the lowest-altitude wavetrain is difficult to characterize because of ambiguities between the wave and changes in the background temperature at the base of the stratosphere. This is the only one of the three wavetrains considered here for which the background has a quadratic term. The damping parameter (0.0223) and the shape of the background temperature profile are rather sensitive to the range of points included in the fit to the wavetrain. Because of the correlation between the wave and background parameters, the main utility of the fit shown here is that it reproduces the gross structure of the complicated lower stratosphere well, with only six parameters. This will allow a comparison against other measurements of this region (such as radio occultations) and models of lower stratospheric temperature profiles (such as the proposed Quasi Quadrennial Oscillation or QQO, e.g., Friedson 1999, Li and Read 2000), and help in interpreting thermal emission spectra. The upper two waves are much less sensitive to the choice of the range included in the fit. The damping parameter for wavetrain B is consistent with a wave whose amplitude is constant with height over the portion of the wave used in the fit, suggesting a critically damped wave, while the amplitude of wavetrain C grows approximately inversely proportionally to density, suggesting an undamped wave. The reasonableness of these interpretations is addressed in Section 4.

3.4 Power spectra

The shape and amplitude of temperature or velocity power spectra due to gravity waves in the terrestrial atmosphere are roughly independent of weather, season, and region of the atmosphere (e.g., VanZandt 1982; Dewan et al. 1984a; Dewan et al. 1984b; Smith *et al.* 1987), and the underlying mechanism for generating this “universal

spectrum" is a topic of active research (e. g. Smith *et al*. 1987, Weinstock 1990, Hines 1991, Gardner 1994, Medvedev and Klassen 1995). Observing whether the universal spectrum extends to other atmospheres may help distinguish between proposed explanations. In this section, we present the power spectral density (PSD) of normalized temperature with respect to vertical wavenumber.

In our altitude range of interest, each accelerometer measured 60 points. We interpolated each accelerometer's data onto an evenly spaced grid of 64 points between 91.2 and 286.3 km altitude, using a cubic spline. The resampling had a negligible impact on the total variance, the criteria used by Pfenninger et al. (1999) for the validity of resampling. To remove the side lobes, we multiply the data by a Hann window ($W = 0.5 - 0.5\cos\left[2\pi(z - z_{\min})/(z_{\max} - z_{\min})\right]$), and then multiply the PSD by 8/3 to compensate for the loss in total power (again following Pfenninger et al. 1999). The power spectrum is calculated by $P_{\Delta T} = \left|\tau_j^* \tau_j\right| 2\Delta z / N$, where Δz is the vertical spacing, N is the number of points, $\tau_j = \sum_{k=0}^{N-1} \Delta T_k \exp\left[-2\pi i j k / N\right]$ is the Fourier transform of ΔT, and τ_j^* is the complex conjugate of τ_j (Dewan 1985). We calculate the PSD of each accelerometer individually, to avoid introducing artifacts arising from small differences in the altitude or temperature scale. We average the logs of the independent PSDs (Pfenninger 1999), increasing the SNR of the final PSD.

The resulting PSD of the normalized temperature profile (ΔT) using both accelerometers is shown in Fig. 7a. The gray region represents the envelope of the PSD of 6400 sample profiles, calculated in the same manner as for Fig. 5a. The PSD calculated from each accelerometer separately (Figs. 7b and 7c) show the same quantitative behavior as that in Fig. 7a. The power spectrum demonstrates some of the impressions described in §3.1, namely peaks at ~10 and ~20-30 km, which may correspond to the short wave trains at 170-210 km and at 230-280, and a general decrease in PSD at shorter vertical wavelengths .

Insert Figure 7 (PSD)

Periodograms of temperature or normalized density in the terrestrial atmosphere have been extensively studied using the modified Desaubies function (e.g., Smith et al. 1987; VanZandt and Fritts 1989; Allen and Vincent 1995), which smoothly makes the transition between the low and high wavenumber portions of the power spectrum. The modified Desaubies function is

$$P_{\Delta T} = a\frac{N^4}{g^2 m_*^3}\frac{\left(m/m_*\right)^s}{1+\left(m/m_*\right)^{s+t}} \tag{3}$$

where N is the Brunt-Väisälä frequency, g is gravity, s and $-t$ are the power indices for low and high wavenumbers, $m = 2\pi/L_z$ is the vertical wavenumber, L_z is the vertical wavelength, m_* is the characteristic wavenumber, and a is a unitless constant.

In figure 6, we show the modified Desaubies function as a smooth curve with the nominal parameters derived from Earth observations and theory, in which a = 1/10 (Smith *et al.* 1987), t = 3 (Dewan and Good 1986; Smith *et al.* 1987), and $m_* = \Gamma\sigma_T/2$ (Collins *et al.* 1996). The long-wavelength exponent (s) is poorly constrained in terrestrial studies by observation. Because the low-m waves are underdamped, s depends on the generating mechanism for gravity waves. We expect that gravity waves are generated differently on Jupiter and on Earth, and therefore s may well be different in the stratospheres of these two planets. We take s=0 in Fig. 6 as assumed by Smith *et al.* (1987), for consistency with their value of a = 1/10. We emphasize that the curve in Fig. 6 is not a fit to the observed PSD, but a blind application of terrestrial theory to the stratosphere of Jupiter via Eq. 3.

If the observed PSD were inconsistent with the nominal values of s, a, m_*, and t, then allowing these to be free parameters would improve the χ^2 per degree of freedom. However, if we fit a general Desaubies spectrum with a, m_*, and t as free parameters, the parameters do not change more than one standard deviation, and the χ^2 per degree of freedom drops. We conclude that the power spectrum of the Galileo ASI is consistent

with those found in the Earth's stratosphere, to within the accuracy of the data. This supports the hypothesis that the gravity wave spectrum is truly universal, applying to atmospheres other than Earth's. In particular, the large-m tail of Jupiter's PSD, which represents the saturated or breaking region of the spectrum, is consistent with the often-noted m^{-3} dependence.

4. Discussion

Based on the above analysis, we pursue the gravity wave interpretation of Jupiter's stratospheric fluctuations. Below, we investigate the effect of breaking waves on the energy budget, place limits on the eddy Prandtl number (Pr, the ratio of the eddy diffusion coefficient for momentum to that for temperature), check plausibility of our interpretations of wavetrains B and C, and compare the observed eddy diffusion coefficient with that predicted by diffusive filtering theory.

Current theories for the cause and behavior of breaking gravity waves include (1) the effect of total wave-induced wind shear on waves with slow horizontal phase speeds (Hines 1991), (2) the onset of convective instability for waves with large temperature derivatives (Dewan and Good 1986, Smith *et al.* 1987), (3) damping of waves where the diffusive timescale (Km^2) is not small compared with a frequency (Lindzen 1981, Gardner, 1994), or (4) the mixing of parcels that do not return to their original position at the end of a wave period (Weinstock 1990, Medvedev and Klassen 1995). Parameterizations based on Hines (1991) or spectral (e.g., multiple wavelength) versions of Lindzen (1981) have both been successfully used in terrestrial Global Circulation Models (GCMs). Because of their simplicity, we concentrate on the spectral Lindzen parameterizations.

The energy flux for undamped waves can be simply described as the product of the energy density and the vertical group velocity (e.g., Gill 1982; Lindzen 1992). The situation becomes more complex when the waves are damped. On the one hand, as waves

are damped, they deposit their energy locally, much of which is expected to finally increase the thermal energy of the background state. On the other hand, damped waves lead to mixing, which effectively acts as an increased diffusion coefficient for diffusion of potential temperature. The interplay between these two effects has been the subject of recent papers on the effect of gravity waves on the thermal structure of Jupiter's thermosphere (Young et al. 1997; Matcheva and Strobel 1999; Hickey et al. 2000). In the thermosphere, the effects of mixing are based on molecular processes such as thermal conduction and molecular diffusion. The equations can be formidable, but the physics of mixing is straightforward.

The situation is entirely different for breaking waves in the stratosphere, dominated by eddy viscosity and eddy conduction. The importance of the competing heating and cooling processes depend on the value of the eddy Prandtl number. Strobel et al. (1985) and Schoeberl et al (1983) discuss the competing effects of energy deposition and diffusion of potential temperature. Their equation for the total heating rate can be written

$$Q = \frac{N^2 K_H}{2}\left[\varepsilon(\mathrm{Pr}+1) + \frac{2c_p}{R}\left(\frac{H}{H_D} - 1\right)\right] \qquad (4)$$

where Q is the gravity wave heating rate in erg g^{-1} s^{-1}, K_H is the eddy diffusion coefficient for heat transport, ε is the efficiency with which gravity wave energy is converted to heat, c_p is the specific heat at constant pressure, R is the gas constant, H is the pressure scale height, and $H_D = K_{zz}/(\partial K_{zz}/\partial z)$ is the scale height of eddy diffusion.

The eddy diffusion coefficient for heat transport (K_H) should equal the eddy diffusion coefficients for the vertical diffusion of constituents (K_{zz}) (e.g., Strobel et al. 1985), which can be estimated from the distribution of minor species. Moses et al. (2002) summarized measurements of K_{zz}. If we assume that the reports of K_{zz} at the homopause refer to $p \approx$ 0.25 μbar, we can fit the reported diffusion coefficients with $K_{zz} = K_0 p^{-H/H_D}$, where K_0 = (2.86±0.77)×10^4 cm^2/s is the eddy diffusion coefficient at 1 mbar, p is the pressure in

mbar, and $H/H_D = 0.61 \pm 0.12$. The efficiency ε is expected to be near unity (Fritts and Dunkerton 1984).

Assuming $K_H \approx K_{zz}$, $Q = 4.3\ p^{-0.61}\ [Pr - 1]$ erg cm^{-2} s^{-1} for Jupiter's stratosphere, with p in mbar. For Pr<1.7, the net effect of the waves is cooling by downward transport of potential temperature, while for $Pr > 1.7$, the net effect of the waves is to heat the atmosphere by direct deposition of the wave energy in the damped waves. Theoretical estimates of Pr range from 1 for waves that are damped uniformly throughout a wave period by pre-existing turbulence fields (Chao and Schoeberl 1984) to $Pr > 20$ for waves experiencing convective instability localized in time and location only near their minimum thermal gradients (Chao and Schoeberl 1984; Strobel et al. 1985; Fritts and Dunkerton 1985; Walterscheid and Schubert 1990). We take the apparent skewness of the thermal gradient distribution as evidence that $Pr > 1$.

We use energy balance considerations to further limit Pr. Jupiter's stratosphere is in approximate radiative equilibrium (Yelle et al. 2001), so we can require than Q not be large compared to the radiative heating and cooling rates. At the top of the stratosphere, at 0.1 mbar, the radiative heating and cooling rates are 430 and 600 erg cm^{-2} s^{-1} respectively. If we impose a conservative 400 erg cm^{-2} s^{-1} as the upper limit on the allowable wave heating rate, then we conclude that $Pr < 4.4$.

At the base of the stratosphere, at 10 mbar, Q ranges from –0.7 erg cm^{-2} s^{-1} to 2.9 erg cm^{-2} s^{-1} for Pr = 1 to 4.4. Since the radiative heating and cooling rates at 10 mbar are 40 and 50 erg cm^{-2} s^{-1} respectively, wave heating/cooling is small compared with the radiative terms in the lower stratosphere.

Having established a range for Pr, we can now address the identification of wavetrains B and C as gravity waves. Linear saturation theory (Lindzen 1981) predicts the growth or damping of waves in the presence of eddy diffusion and vertical shear of horizontal background wind. The shear ($|du_0/dz|$) is unimportant when $L_z >> |du_0/dz|(3H)/(2\pi N)$. For the expected shears of ~4.1×10^{-4} s^{-1} (Li and Read 2000),

this is satisfied for vertical wavelengths >> 0.29 km. Therefore, wind shear can be ignored when calculating the critical damping coefficient for all wavelengths detectable by the Galileo ASI, including those of wavetrains B and C.

Linear saturation theory predicts waves will be critically damped (i.e., constant amplitude) when the period equals the critical period $\omega_{crit} = 2\,KH\,(2\pi/L_z)^3$, where $K = (K_H + K_M)/2$ is the effective eddy diffusion coefficient for wave damping and K_M is the eddy diffusion coeffienct for momentum transport (related to K_H by the Prandtl number, $Pr = K_M/K_H$). Wavetrain B will be critically damped if ω_B equals 8.8×10^{-5} to 2.4×10^{-4} s^{-1} for Pr = 1 to 4.4. Similarly, wavetrain C is undamped for $Pr < 4.4$ (at least below the altitude where it becomes convectively unstable) if $\omega_C > 1.1\times10^{-4}$ s^{-1}.

These frequencies can be compared with the Coriolis frequency, f (4.0×10^{-5} s^{-1}) and the Brunt-Väisällä frequency, N (1.7×10^{-2} s^{-1}). We can also estimate a "typical" frequency by assuming a form for the frequency power spectrum. In the Earth's atmosphere, the frequency power spectrum is found to be proportional to ω^{-p} for $f < \omega < N$, with $p \approx 5/3$ (e.g., VanZandt 1982; Fritts 1989). The average (e.g., power-weighted) ω is defined by

$$\overline{\omega} = \frac{\int_f^N \omega^{1-p} d\omega}{\int_f^N \omega^{-p} d\omega} = 2\frac{N^{2/3} f^{2/3}}{N^{1/3} + f^{1/3}} \qquad (5)$$

where the right-most expression is for p = 5/3. For the values of f and N in Jupiter's stratosphere, this yields $\overline{\omega}$=5.3×10^{-4} s^{-1}. Since $\omega_B \approx \overline{\omega}$ and $\overline{\omega} > \min(\omega_C)$, we conclude that wavetrains B and C are, indeed, critically damped and undamped waves, respectively.

Since breaking gravity waves are often postulated to be the source of eddy mixing (e.g., Lindzen 1981; Medvedev and Klassen 1995), it would be useful if we can show that the eddy diffusion coefficient could be calculated from the observed temperature fluctuations. To this end, we employed the diffusive filtering theory of Gardner (1994), which treats a spectrum of waves as a superposition of non-interacting linear waves. In

this parameterization, the critical wavelength (L_*) and effective eddy diffusion coefficient (K) both increase with decreasing pressure, with $H/H_D = 2/(s+3)$ and $K=f(2\pi/L_*)^2$. For s in the range between 0 and 1, H/H_D is between 0.5 and 0.67, agreeing with the estimated value of $H/H_D = 0.61\pm0.12$. Because our analysis calculates a single PSD for the entire stratosphere, we have no observational information on the variation of L_* with altitude. The value of L_* derived in Section 3.4 (30.3 km) must be considered a characteristic value for the stratosphere as a whole. Diffusive filtering theory predicts $KH = (2/(Pr+1))\times9.3\times10^6$ cm^2/s if L_*=30.3 km. For $1< Pr \leq 4.4$, the predicted eddy diffusion coefficient is larger than the largest observed eddy diffusion over our altitudes of interest. We conclude that the diffusive filtering theory overestimates the eddy diffusion coefficients in Jupiter's stratosphere.

5. Summary and conclusions

Our results can be summarized as follows:

1. Temperature fluctuations in Jupiter's stratosphere are not due to either measurement error or isotropic turbulence. Based on analogy with the terrestrial stratosphere, we interpret these fluctuations as due to a spectrum of breaking gravity waves.

2. While probe accelerometer measurements are highly sensitive to horizontal variations (which would be aliased as overlarge vertical gradients), occultations are insensitive to horizontal density variations (as they average refractivity along a line-of-sight through the atmosphere). The qualitative agreement between the probe and occultation profiles could be taken as a validation of these different techniques.

3. The aspect ratio (ratio of horizontal to vertical scales) is > 8.

4. Power spectra of temperature with respect to vertical wavenumber for the terrestrial atmosphere are generally independent of weather, season, and region of the atmosphere. The ASI observations are consistent with this "universal" spectrum,

suggesting that it is truly universal, since it applies to an atmosphere with different values for N and g. This further suggests that the underlying physical causes of gravity wave saturation are similar, and that parameterizations developed for terrestrial modeling and observations can be applied on Jupiter, and presumably elsewhere in the solar system.

5. The diffusive filtering theory (Gardner 1994) cannot be used to predict eddy diffusion coefficients in Jupiter's stratosphere, and, by extension, in the stratospheres on the other giant planets. If a parameterization can be found or devised that does predict eddy diffusion coefficients on the Earth and the giant planets, it will prove an important test for distinguishing among the current competing theories of gravity wave saturation.

6. The eddy Prandtl number Pr (the ratio of the momentum diffusion coefficient to the thermal diffusion coefficient) in Jupiter's stratosphere lies in the range $1<Pr\leq 4.4$.

7. Wave heating or cooling is probably unimportant in Jupiter's lower stratosphere (e.g., near 10 mbar). In Jupiter's upper stratosphere (e.g., near 3 μbar), wave heating or cooling is likely to be very important unless $Pr \approx 1.7$. For $Pr<1.7$, waves cause net cooling, and for $Pr > 1.7$, they cause net heating.

Acknowledgments

This paper is dedicated to our friend and colleague, Al Seiff. The work was supported, in part, by NASA's Planetary Atmsopheres program, through RTOP 344-33-20-03 (REY) and NEG5-9214 (RVYT). Hans Meyr and Jeff Forbes gave key references.

References

Allen, S. J. and R. A. Vincent 1995. Gravity wave activity in the lower atmosphere: seasonal and latitudinal variations. *J. G. R.* **100**, 1327-1350.

Allison, M. 1990. Planetary waves in Jupiter's equatorial atmosphere. *Icarus* **83**, 282-307.

Chao, W. C. and M. R. Schoeberl 1984. On the linear approximation of gravity wave saturation in the mesosphere. *J. Atmos. Sci.***41**, 1893-1898.

Collins, R., X. Tao, and C. Gardner 1996. Gravity wave activity in the upper mesosphere over Urbana, Illinois: lidar observations and analysis of gravity wave propagation models. *J. Atmos. and Terr. Phys.* **58**, 1905-1926.

Cooray, A. R., J. L. Elliot, A. S. Bosh, L. A. Young, and M. A. Shure 1998. Stellar Occultation Observations of Saturn's North-Polar Temperature Structure. *Icarus* **132**, 298-310.

Dewan, E. M., N. Grossbard, A. F. Quesda, and R. E. Good 1984a. Spectral analysis of 10m resolution scalar velocity profiles in the stratosphere. *G. R. L.* **11**, 80-83.

Dewan, E. M., N. Grossbard, A. F. Quesda, and R. E. Good 1984b. Spectral analysis of 10m resolution scalar velocity profiles in the stratosphere: Correction. *G. R. L.* **11**, 624.

Dewan, E. M. 1985. On the nature of atmospheric waves and turbulence. *Radio Science*, **20**, 1301.

Dewan, E. M. and R. E. Good 1986. Saturation and the "universal" spectrum for vertical profiles of horizontal scalar winds in the atmosphere. *JGR* **91**, 2742.

French, R. J. and P. J. Gierasch 1974. Waves in the Jovian upper atmosphere. *J. Atmos. Sci.* **31**, 1707-1712.

Friedson, A. J. 1999. New Observations and Modelling of a QBO-Like Oscillation in Jupiter's Stratosphere. *Icarus* **137**, 34-55.

Fritts, DC 1989. A review of gravity wave saturation processes, effects, and variability in the middle atmosphere. *Pure. Appl. Geophys.* **130** 343-371.

Fritts, D. C. and T. J. Dunkerton 1984. A quasi-linear study of gravity wave saturation and self-acceleration. *J. Atmos. Sci.* **41**, 3272-3289.

Fritts, D. C. and T. J. Dunkerton 1985. Fluxes of heat and constituents due to convectively unstable gravity waves. *J. Atmos. Sci.* **42**, 549-556.

Gage, K. S. and G. D. Nastrom 1985. On the spectrum of atmospheric velocity fluctuations seen by MST/ST radar and their interpretation. *Radio Sci* **20**, 1339-1347.

Gardner, C. S. 1994. Diffusive filtering theory of gravity-wave spectra in the atmosphere. *JGR* **99**, 20601-20622.

Gill, A. E. 1982. *Atmosphere-ocean dynamics.* Academic Press, New York.

Hines, C. O. 1991. The saturation of gravity waves in the middle atmosphere. Part II: development of doppler-spread theory. *J. Atmos. Sci.* **48**, 1360-1379.

Jokipii J. R. and W. B. Hubbard 1977. Stellar occultations by turbulent planetary atmospheres: the β Scorpii events. *Icarus*, **30**, 537-550.

Li, X. and P. L. Read 2000. A mechanistic model of the quasi-quadrennial oscillation in Jupiter's stratosphere. *P&SS* **48**, 637-669.

Lindel, G. F, and 11 colleagues 1981. The atmosphere of Jupiter: an analysis of the Voyager radio occultation measurements. *J. G. R.* **86**, 8721-8727.

Lindzen, R. S. 1981. Turbulence and stress owing to gravity wave and tidal breakdown. *JGR* **86**, 9707-9714.

Lindzen, R. S. 1992. *Dynamics in Atmospheric Physics.* Cambridge University Press, New York.

Matcheva, K. I., and D. F. Strobel 1999. Heating of Jupiter's thermosphere by dissipation of gravity waves due to molecular viscosity and heat conduction. *Icarus* **140**, 328-340.

Medvedev, A. S. and G. P. Klassen, 1995. Vertical evolution of gravity wave spectra and the parameterization of associated wave drag. *JGR* **100**, 25841-25853.

Moses, J. I. and 9 collaborators, 2002. The stratosphere of Jupiter. In *Jupiter: Planet, Satellites, and Magnetosphere.* F. Bagenal, T. Dowling, and W. McKinnon, eds. Cambridge University Press, New York.

Pfenninger, M, A. Liu, G. Papen, and C. Gardner 1999. Gravity wave characteristics in the lower atmosphere at South Pole. *JGR* **104** 5963-5984.

Press, W. H., S. A. Teukolsky, W. T. Vetterling and B. P. Flannery 1992. *Numerical Recipes*. Cambridge University Press, New York.

Roques, F. and 16 colleagues 1994. Neptune's upper stratosphere, 1983-1990: ground-based stellar occultation observations III. Temperature profiles. *Astron, & Astrophys.* **288**, 985-1011.

Seiff, A. and T. C. D. Knight 1992. The Galileo Probe Atmosphere Structure Instrument. *Space Science Reviews* **60**, 203-232.

Seiff, A., D. B. Kirk, T. C. D. Knight, R. E. Young, J. D. Mihalov, L. A. Young, F. S. Milos, G. Schubert, R. C. Blanchard, and D. Atkinson 1998. Thermal structure of Jupiter's atmosphere near the edge of a 5-μm hot spot in the north equatorial belt. *J. Geophys. Res.* **103**, 222857-22890.

Sicardy, B. and 23 colleagues 1999. The Structure of Titan's Stratosphere from the 28 Sgr Occultation. *Icarus* **142**, 357-390.

Smtih, S. A., D. C. Fritts, and T. E. VanZandt 1987. Evidence for a saturated spectrum of gravity waves. *J. Atmos. Sci.* **44**, 1404-1410.

Strobel, D. F., J. P. Apruzese, and M. R. Schoeberl 1985. Energy balance constraints on gravity wave induced eddy diffusion in the mesosphere and lower thermosphere. *J. Geophys. Res.* **90**, 13067–13072.

VanZandt, T. E. 1982. A universal spectrum of buoyancy waves in the atmosphere. *GRL* **9**, 575-578.

VanZandt, T. E. and D. C. Fritts 1989. A theory of enhanced saturation of the gravity wave spectrum due to increases in atmospheric stability. *Pure & Appl. Geophys.* **130**, 399-420.

Walterscheid, R. L. and G. Schubert 1990. Nonlinear evolution of an upward propagating gravity wave: overturning, convection, transience, and turbulence. *J. Atmos. Sci.* **47**, 101-125.

Weinstock, J. 1990. Saturated and unsaturated spectra of gravity waves and scale-dependent diffusion. *J. Atmos. Sci.* **47**, 2211-2225.

Yelle, R. V., C. A. Griffith, and L. A. Young 2001. Structure of the Jovian stratosphere at the Galileo probe entry site. *Icarus* 152, 331-346.

Young, L. A., R. V. Yelle, R. E. Young, A. Seiff, and D. B. Kirk 1997. Gravity waves in Jupiter's thermosphere. *Science* **276**, 108-111.

Figure 1. Overview of Jupiter's thermal profile derived from the z1 accelerometer of the Galileo ASI during the entry phase. This paper concentrates on region between 90 and 290 km (filled circles).

Figure 2. Fractional variations in temperature (solid), density (dashed), and acceleration (dotted). For ease of comparison, the negative of the density and acceleration variations are plotted. The digitization error for the acceleration variations, with the full width of the error bars indicating the accelerometer resolution. The observed fluctuations are generally larger than the digitization error.

Figure 3. Jovian temperature fluctuations between the altitudes of 90 and 290 km derived from the z1 (circle) and z2 (square) accelerometer measurements during the entry phase of the Galileo ASI. Arrows indicate points that were smoothed in S98, and are reinstated here. Error bars represent measurement error, dominated by the digitization error (e.g., resolution) of the accelerometers (see text).

Figure 4. Temperature gradients in Jupiter's stratosphere, between the altitudes of 90 and 290 km derived from the z_1 (circle) and z_2 (square) accelerometer measurements during the entry phase of the Galileo ASI. Error bars indicate measurement error, dominated by the digitization error (e.g., resolution) of the accelerometers. Dotted vertical lines indicate $\pm\Gamma$, where $\Gamma=g/c_p$ is the adiabatic gradient.

Fig. 5. Histogram of temperature gradients, with bin widths one-fifth of the adiabatic lapse rate (Γ). (A) Histogram of temperatures from both accelerometers, Gray regions represent the uncertainty in each bin from a Monte-Carlo simulation of the measurement errors (see text). (B) Histogram using only accelerometer z_1. (C) Same for z_2. Vertical dashed lines indicate Γ, 0, and $-\Gamma$. Note that the distribution is skewed, and bounded on the negative side by the adiabatic lapse rate.

Fig. 6. Three wave trains in the Galileo ASI data.

Fig. 7. Power spectral densities (PSD) of normalized temperature. (A) Average PSD of the two accelerometers. Gray regions represent the uncertainty at each vertical wavelength from a Monte-Carlo simulation of the measurement errors (see text). (B) PSD using only accelerometer z_1. (C) Same for z_2. In all three plots, the smooth curve is the "terrestrial analog" Desaubies function, as described in Section 3.3.

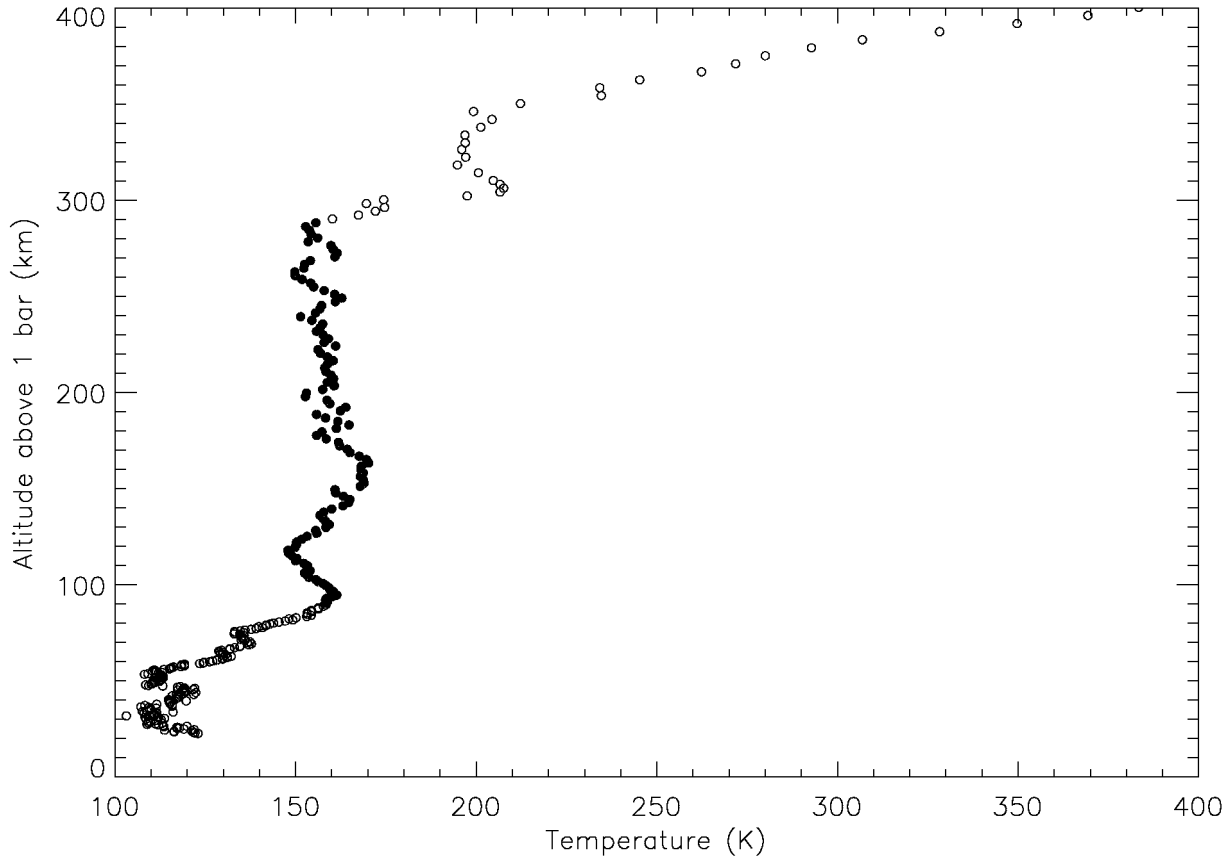
400
300
200
100
0
Altitude above 1 bar (km)
100
150
200
250
300
350
400
Temperature (K)

Figure 1

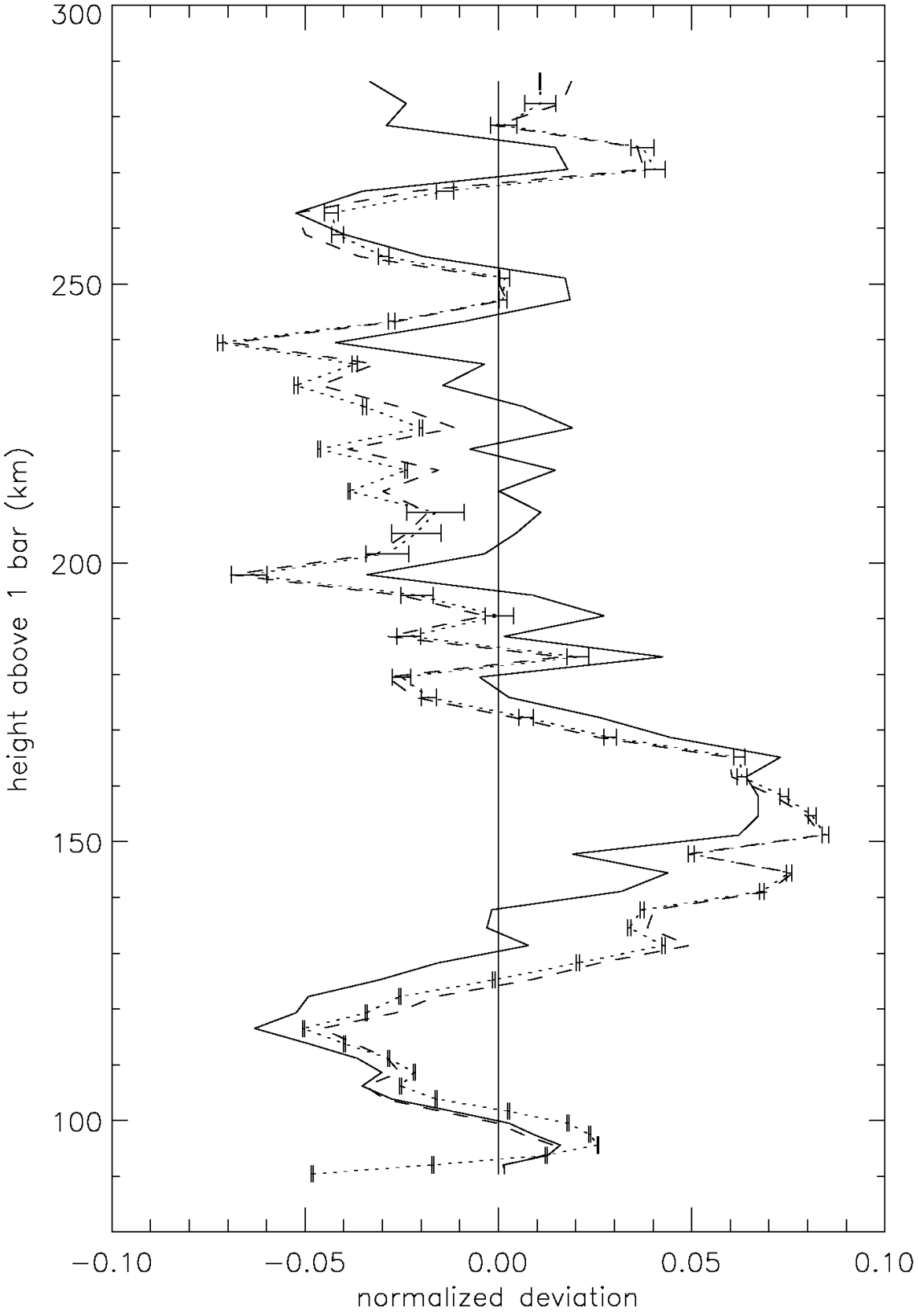
300
250
200
150
100
height above 1 bar (km)
−0.10
−0.05
0.00
0.05
0.10
normalized deviation

Figure 2

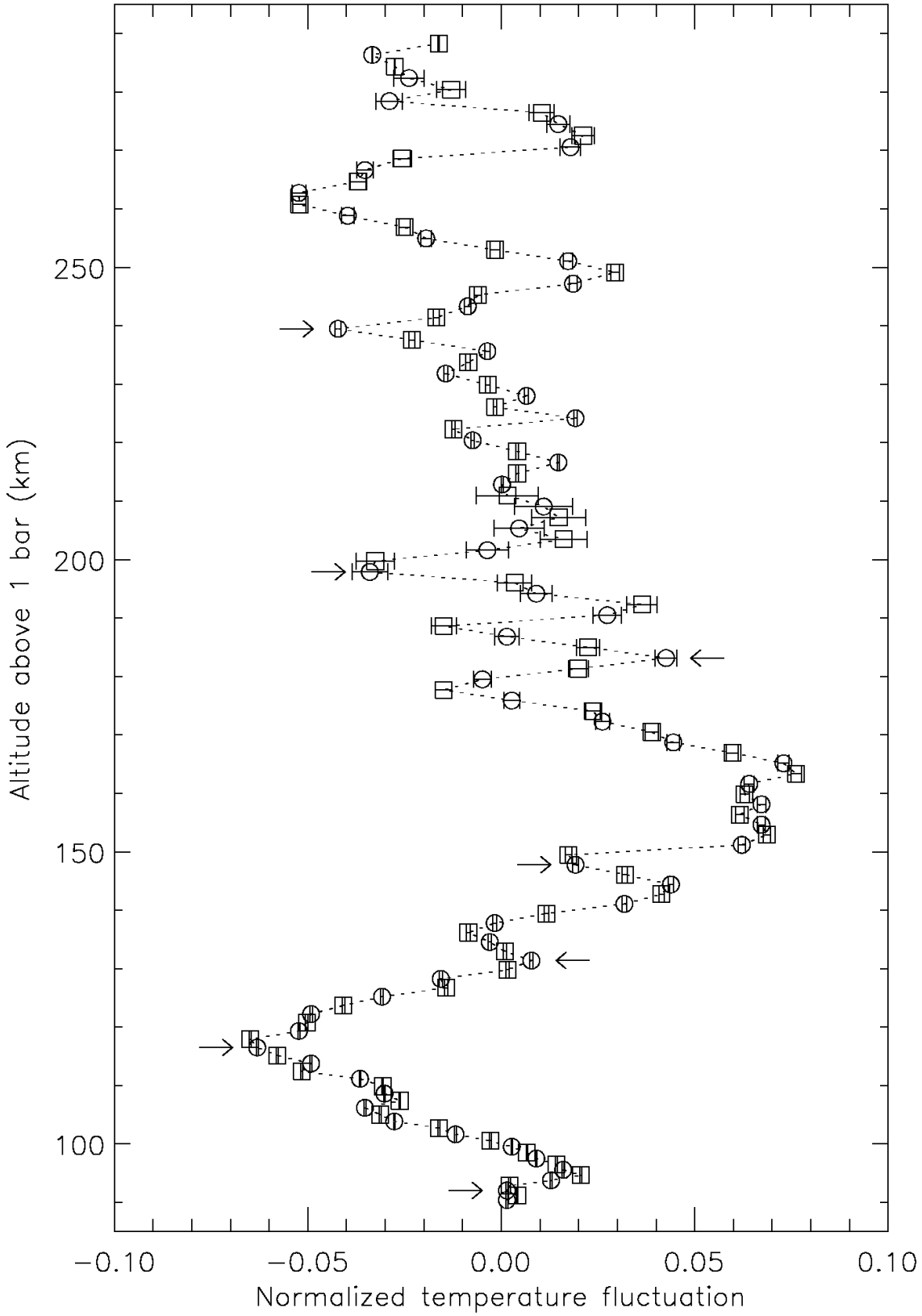
Altitude above 1 bar (km)
250
200
150
100
−0.10
−0.05
0.00
0.05
0.10
Normalized temperature fluctuation

Figure 3

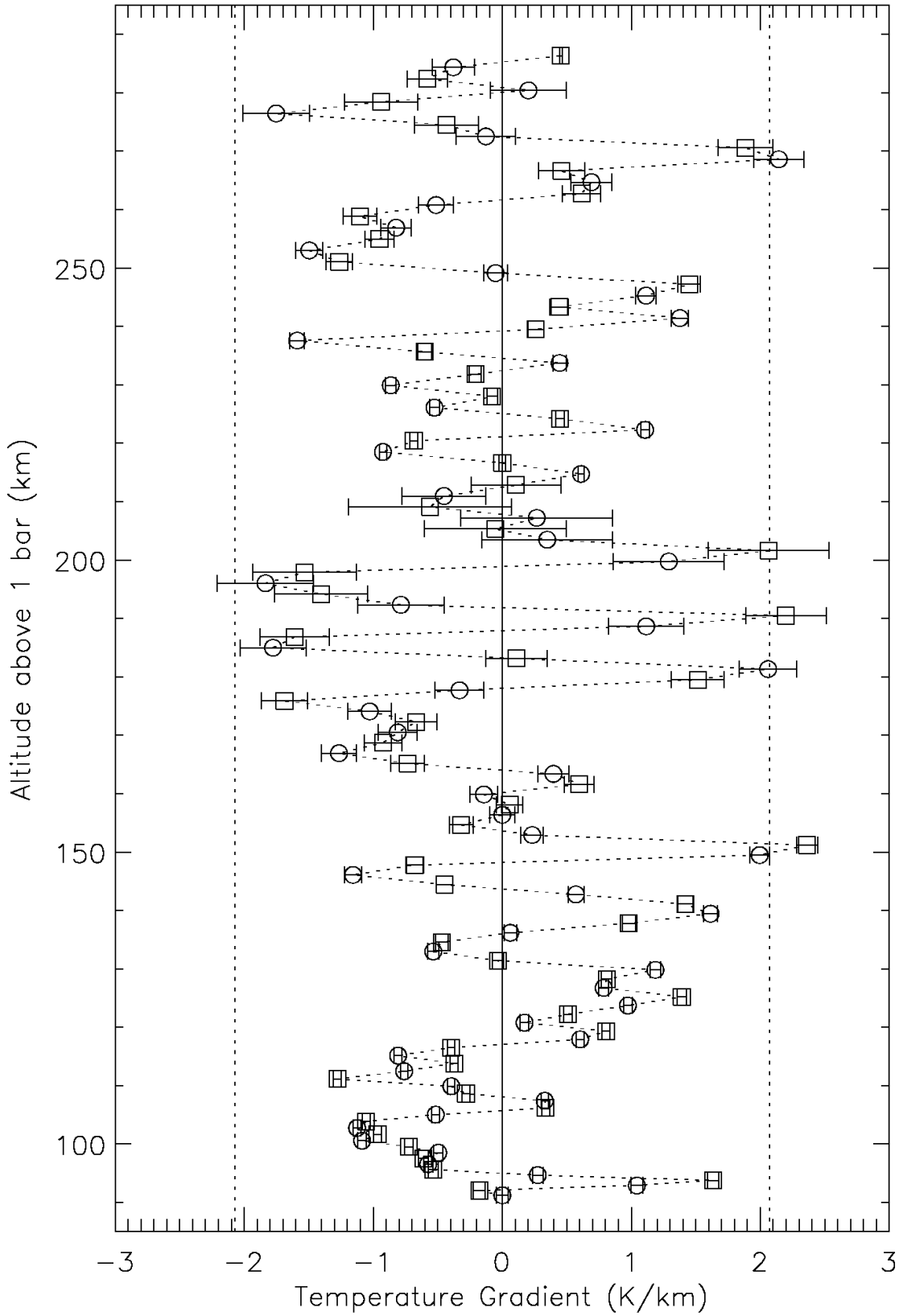
Altitude above 1 bar (km)
250
200
150
100
−3
−2
−1
0
1
2
3
Temperature Gradient (K/km)

Figure 4

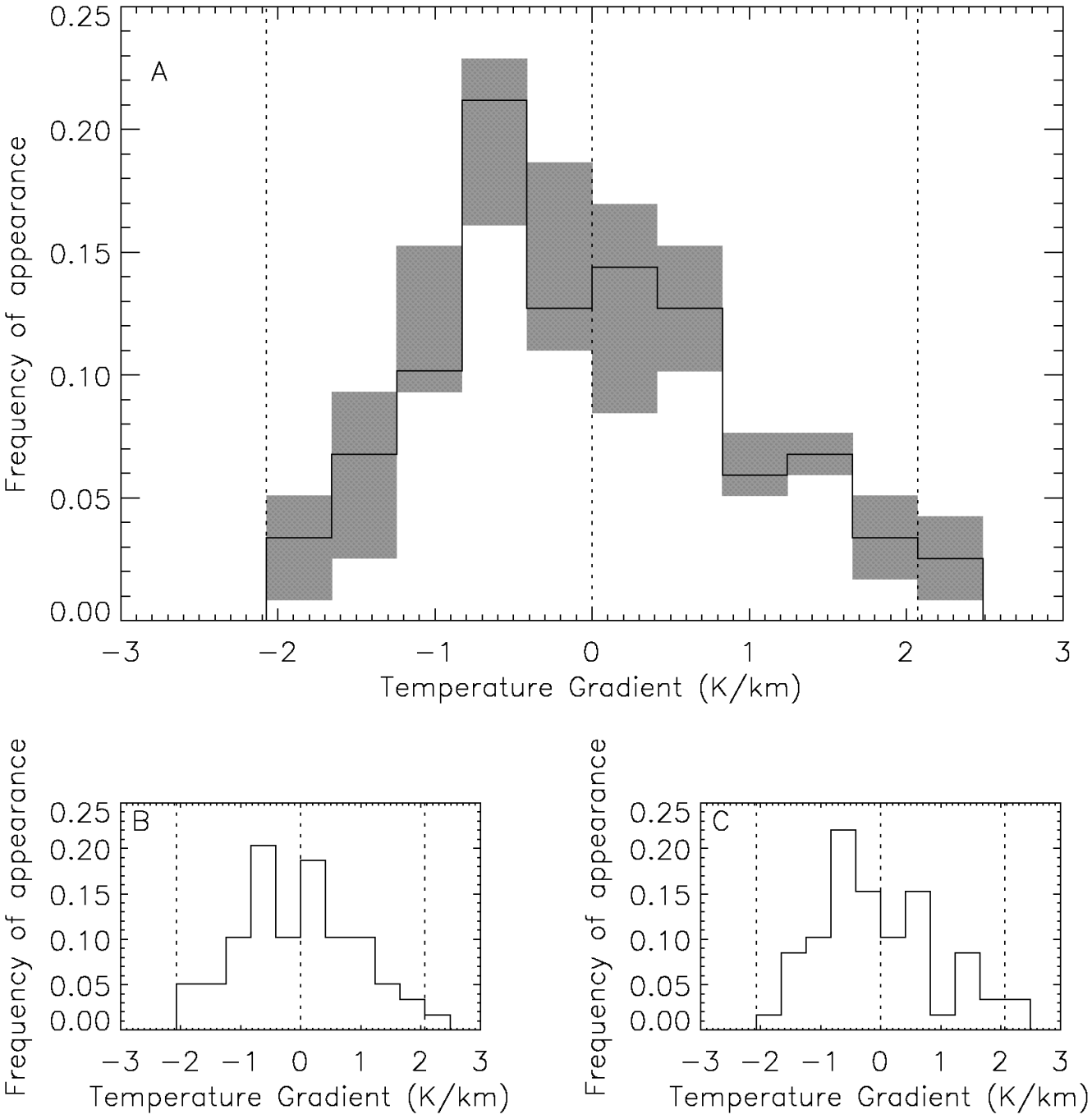
A
B
C
Frequency of appearance
Temperature Gradient (K/km)
0.25
0.20
0.15
0.10
0.05
0.00
−3
−2
−1
0
1
2
3

Figure 5

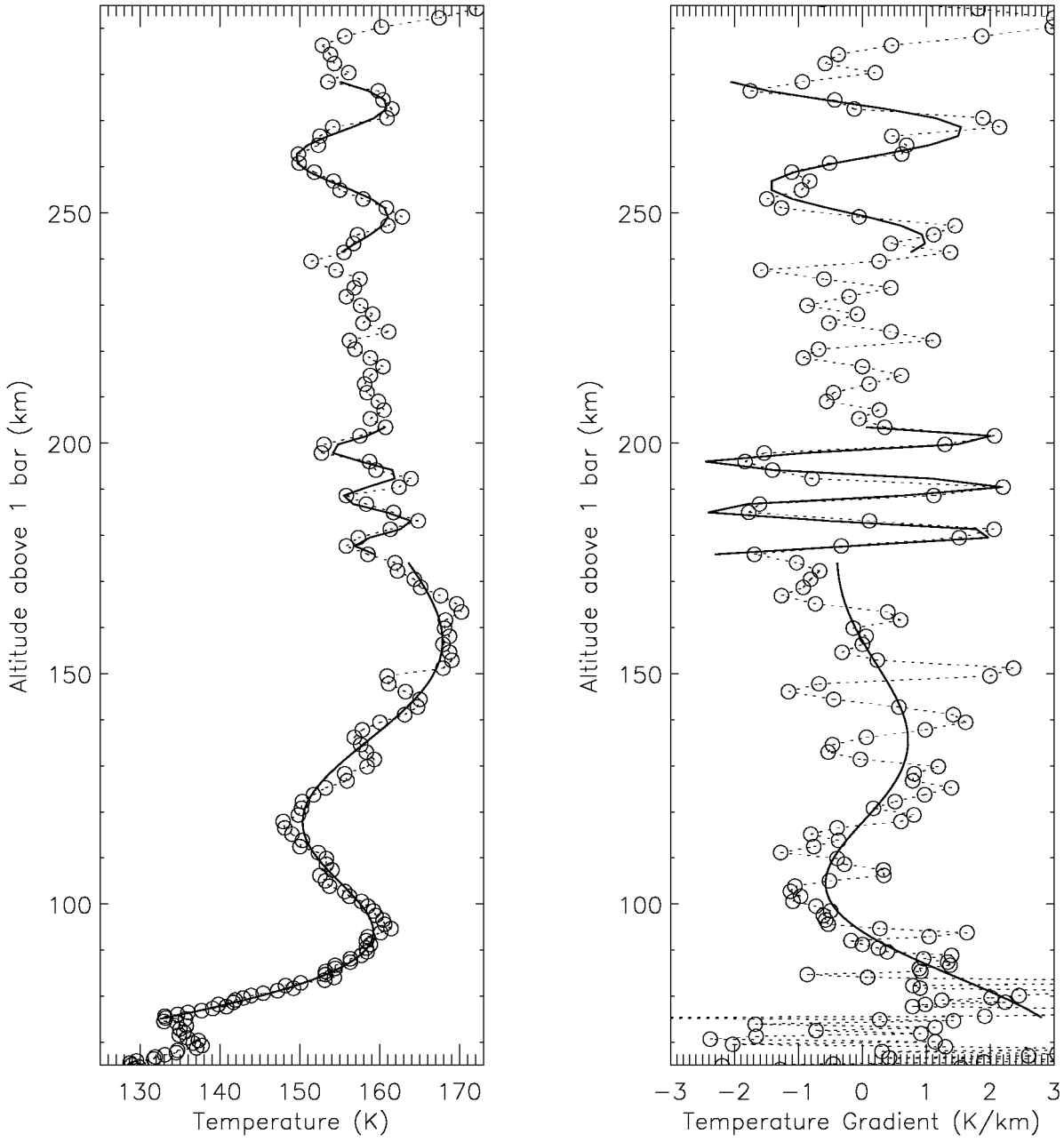
Altitude above 1 bar (km)
250
200
150
100
130
140
150
160
170
Temperature (K)
Altitude above 1 bar (km)
250
200
150
100
−3
−2
−1
0
1
2
3
Temperature Gradient (K/km)

Figure 6

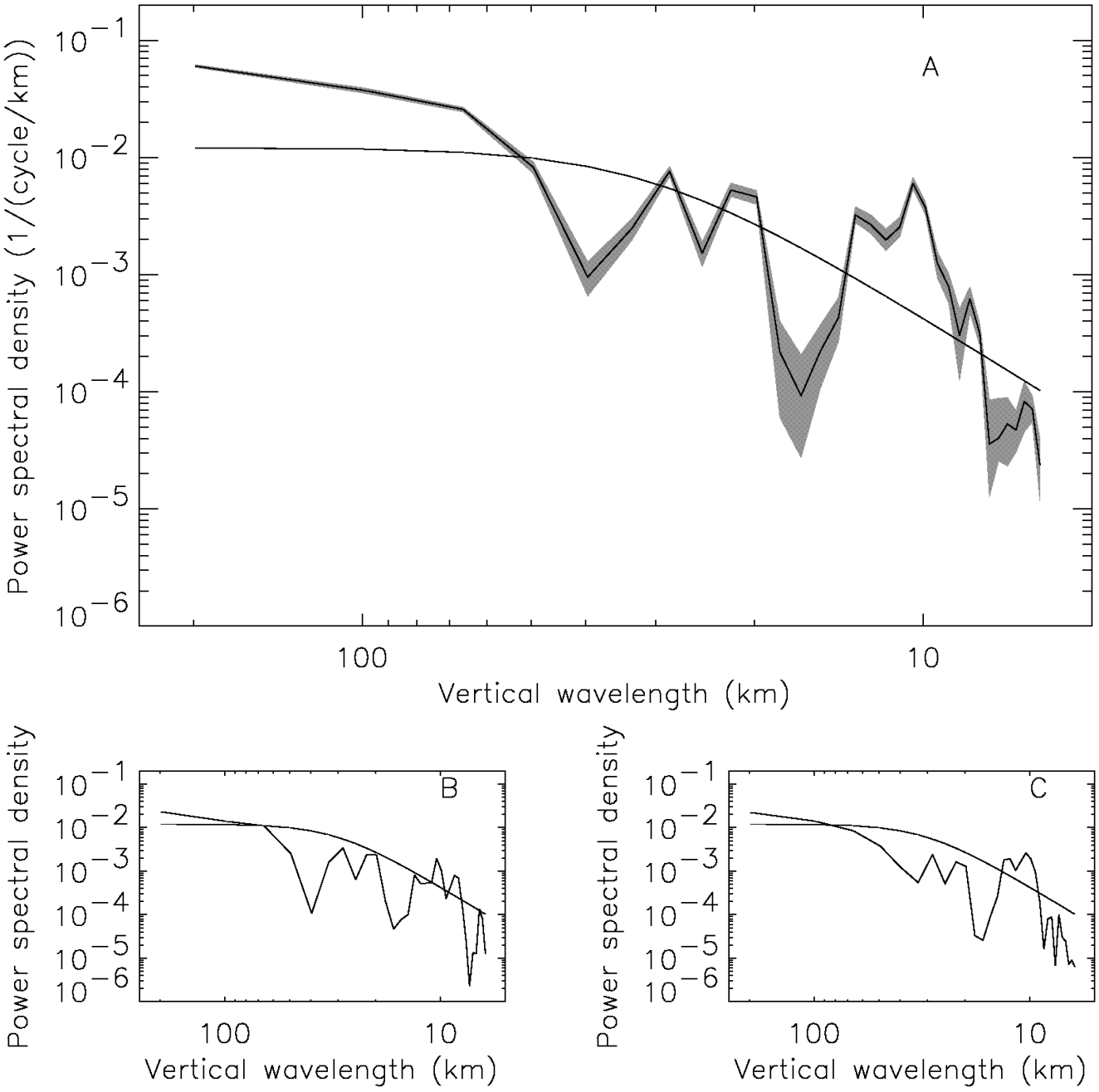
A
B
C
Power spectral density (1/(cycle/km))
Power spectral density
Vertical wavelength (km)
100
10
10^{-1}
10^{-2}
10^{-3}
10^{-4}
10^{-5}
10^{-6}

Figure 7

Table I: Accelerometer data for sensor z_1

Time before start of descent mode t (s)	Vertical velocity v_z (km/s)	Altitude z (km)	Density ρ (kg/m^3)	Pressure p (mb)	Temper-ature T (K)	Molecular weight μ	Fractional acceleration resolution ε_a
-147.742	47.4605	326.453	.1311E-06	.9387E-03	196.0	2.275	1.1E-03
-147.117	47.4619	322.399	.1487E-06	.1069E-02	197.1	2.279	9.6E-04
-146.492	47.4632	318.354	.1717E-06	.1218E-02	194.8	2.282	8.4E-04
-145.867	47.4644	314.320	.1901E-06	.1386E-02	200.6	2.285	7.7E-04
-145.242	47.4655	310.294	.2115E-06	.1572E-02	204.7	2.289	7.1E-04
-144.617	47.4665	306.278	.2362E-06	.1778E-02	207.6	2.292	6.5E-04
-143.992	47.4675	302.272	.2816E-06	.2014E-02	197.5	2.295	5.7E-04
-143.367	47.4682	298.275	.3780E-06	.2320E-02	169.6	2.297	4.7E-04
-142.742	47.4688	294.288	.4318E-06	.2688E-02	172.1	2.298	4.2E-04
-142.117	47.4691	290.310	.5409E-06	.3132E-02	160.2	2.299	3.5E-04
-141.492	47.4691	286.342	.6679E-06	.3687E-02	152.8	2.301	2.9E-04
-140.867	47.4688	282.384	.7803E-06	.4345E-02	154.3	2.302	8.0E-03
-140.242	47.4681	278.435	.9250E-06	.5124E-02	153.5	2.303	6.8E-03
-139.617	47.4671	274.496	.1040E-05	.6013E-02	160.4	2.305	6.1E-03
-138.992	47.4656	270.566	.1211E-05	.7024E-02	160.9	2.305	5.3E-03
-138.367	47.4635	266.646	.1501E-05	.8250E-02	152.5	2.306	4.3E-03
-137.742	47.4606	262.736	.1805E-05	.9742E-02	149.8	2.306	3.6E-03
-137.117	47.4568	258.836	.2103E-05	.1150E-01	151.8	2.307	3.1E-03
-136.492	47.4522	254.946	.2424E-05	.1353E-01	155.0	2.307	2.7E-03
-135.867	47.4467	251.066	.2733E-05	.1583E-01	160.8	2.308	2.4E-03
-135.242	47.4402	247.196	.3184E-05	.1846E-01	161.0	2.308	2.1E-03
-134.617	47.4322	243.336	.3821E-05	.2157E-01	156.7	2.308	1.8E-03
-133.992	47.4221	239.486	.4650E-05	.2535E-01	151.4*	2.308	1.5E-03
-133.367	47.4102	235.647	.5239E-05	.2971E-01	157.5	2.308	1.3E-03
-132.742	47.3961	231.819	.6200E-05	.3477E-01	155.8	2.308	1.1E-03
-132.117	47.3795	228.001	.7092E-05	.4062E-01	159.1	2.308	9.6E-04
-131.492	47.3605	224.194	.8153E-05	.4729E-01	161.1	2.308	8.4E-04
-130.867	47.3377	220.398	.9765E-05	.5517E-01	156.9	2.309	7.1E-04
-130.242	47.3111	216.614	.1113E-04	.6426E-01	160.4	2.309	6.2E-04
-129.617	47.2800	212.842	.1315E-04	.7484E-01	158.1	2.309	5.3E-04
-128.992	47.2436	209.082	.1515E-04	.8710E-01	159.8	2.309	1.5E-02
-128.367	47.2012	205.334	.1772E-04	.1013E+00	158.8	2.309	1.3E-02
-127.742	47.1517	201.600	.2078E-04	.1178E+00	157.5	2.309	1.1E-02
-127.117	47.0921	197.879	.2505E-04	.1377E+00	152.7*	2.309	9.2E-03
-126.492	47.0238	194.173	.2792E-04	.1603E+00	159.5	2.309	8.3E-03
-125.867	46.9471	190.482	.3176E-04	.1856E+00	162.4	2.309	7.3E-03
-125.242	46.8571	186.806	.3778E-04	.2153E+00	158.3	2.309	6.2E-03
-124.617	46.7556	183.147	.4193E-04	.2487E+00	164.8*	2.309	5.6E-03
-123.992	46.6363	179.506	.5087E-04	.2879E+00	157.3	2.309	4.6E-03
-123.367	46.4963	175.884	.5852E-04	.3338E+00	158.5	2.309	4.1E-03
-122.742	46.3380	172.282	.6606E-04	.3856E+00	162.2	2.309	3.6E-03
-122.117	46.1598	168.703	.7473E-04	.4440E+00	165.1	2.309	3.2E-03
-121.492	45.9620	165.147	.8334E-04	.5088E+00	169.6	2.309	2.9E-03
-120.867	45.7382	161.615	.9614E-04	.5821E+00	168.2	2.309	2.5E-03
-120.242	45.4845	158.111	.1096E-03	.6654E+00	168.7	2.309	2.3E-03
-119.617	45.1981	154.635	.1252E-03	.7597E+00	168.7	2.309	2.0E-03

-118.992	44.8756	151.191	.1433E-03	.8662E+00	167.9	2.309	1.8E-03
-118.367	44.4997	147.782	.1708E-03	.9907E+00	161.1*	2.309	1.5E-03
-117.742	44.0776	144.410	.1905E-03	.1131E+01	165.0	2.309	1.4E-03
-117.117	43.6069	141.080	.2195E-03	.1289E+01	163.1	2.309	1.2E-03
-116.492	43.0657	137.796	.2589E-03	.1471E+01	157.8	2.309	1.1E-03
-115.867	42.4523	134.562	.2960E-03	.1679E+01	157.6	2.309	9.4E-04
-115.242	41.7770	131.383	.3331E-03	.1910E+01	159.3*	2.309	8.6E-04
-114.617	41.0220	128.264	.3875E-03	.2170E+01	155.6	2.309	7.7E-04
-113.992	40.1759	125.211	.4469E-03	.2464E+01	153.2	2.309	6.8E-04
-113.367	39.2315	122.231	.5172E-03	.2797E+01	150.3	2.309	6.2E-04
-112.742	38.1945	119.329	.5879E-03	.3169E+01	149.8	2.309	5.7E-04
-112.117	37.0629	116.513	.6715E-03	.3580E+01	148.1*	2.309	5.2E-04
-111.492	35.8555	113.788	.7447E-03	.4027E+01	150.3	2.309	4.9E-04
-110.867	34.5926	111.158	.8221E-03	.4505E+01	152.3	2.309	4.7E-04
-110.242	33.2806	108.626	.9087E-03	.5012E+01	153.3	2.309	4.6E-04
-109.617	31.9193	106.195	.1012E-02	.5553E+01	152.5	2.309	4.4E-04
-108.992	30.5194	103.868	.1108E-02	.6125E+01	153.7	2.309	4.3E-04
-108.367	29.1193	101.646	.1195E-02	.6717E+01	156.2	2.309	4.4E-04
-107.742	27.7300	99.528	.1284E-02	.7325E+01	158.5	2.309	4.4E-04
-107.117	26.3602	97.511	.1385E-02	.7950E+01	159.5	2.309	4.5E-04
-106.492	25.0191	95.594	.1486E-02	.8587E+01	160.6	2.309	4.6E-04
-105.867	23.7100	93.774	.1604E-02	.9239E+01	160.1	2.309	4.7E-04
-105.242	22.4298	92.048	.1740E-02	.9909E+01	158.3*	2.309	4.8E-04
-104.617	21.1923	90.413	.1859E-02	.1059E+02	158.3	2.309	5.0E-04
-103.992	20.0064	88.865	.1988E-02	.1128E+02	157.7	2.309	5.3E-04
-103.367	18.8715	87.401	.2130E-02	.1198E+02	156.3	2.309	5.5E-04
-102.742	17.7867	86.015	.2283E-02	.1269E+02	154.4	2.309	5.8E-04
-102.117	16.7547	84.705	.2432E-02	.1341E+02	153.2	2.309	6.1E-04
-101.492	15.7847	83.467	.2564E-02	.1412E+02	153.1*	2.309	6.5E-04
-100.867	14.8593	82.294	.2784E-02	.1485E+02	148.2	2.309	6.7E-04
-100.242	13.9827	81.186	.2943E-02	.1559E+02	147.2	2.309	7.2E-04
-99.617	13.1548	80.137	.3154E-02	.1633E+02	143.9	2.309	7.6E-04
-98.992	12.3741	79.144	.3344E-02	.1708E+02	141.9	2.309	8.1E-04
-98.367	11.6409	78.204	.3545E-02	.1783E+02	139.8	2.309	8.6E-04
-97.742	10.9580	77.312	.3711E-02	.1858E+02	139.1	2.309	9.3E-04
-97.117	10.3178	76.467	.3951E-02	.1933E+02	136.0	2.309	9.8E-04
-96.492	9.7129	75.664	.4195E-02	.2009E+02	133.1	2.309	1.0E-03

* Smoothed in S98 (see text).

Table II: Accelerometer data for sensor z_2

Time before start of descent mode t (s)	Vertical velocity v_z (km/s)	Altitude z (km)	Density ρ (kg/m^3)	Pressure p (mb)	Temper-ature T (K)	Molecular weight μ	Fractional acceleration resolution ε_a
-144.930	47.4660	308.285	.2234E-06	.1675E-02	206.6	2.290	6.8E-04
-144.305	47.4670	304.274	.2526E-06	.1891E-02	206.6	2.293	6.1E-04
-143.680	47.4679	300.273	.3432E-06	.2166E-02	174.4	2.296	5.0E-04
-143.055	47.4685	296.280	.3972E-06	.2508E-02	174.6	2.297	4.5E-04
-142.430	47.4690	292.298	.4803E-06	.2908E-02	167.4	2.299	3.8E-04
-141.805	47.4692	288.325	.6058E-06	.3406E-02	155.6	2.300	3.2E-04
-141.180	47.4690	284.362	.7225E-06	.4013E-02	153.8	2.301	2.7E-04
-140.555	47.4685	280.408	.8383E-06	.4724E-02	156.1	2.303	7.5E-03
-139.930	47.4677	276.464	.9610E-06	.5541E-02	159.8	2.304	6.6E-03
-139.305	47.4665	272.530	.1112E-05	.6473E-02	161.5	2.305	5.8E-03
-138.680	47.4647	268.605	.1368E-05	.7596E-02	154.1	2.305	4.8E-03
-138.055	47.4622	264.690	.1629E-05	.8945E-02	152.3	2.306	4.0E-03
-137.430	47.4589	260.785	.1956E-05	.1056E-01	149.9	2.306	3.4E-03
-136.805	47.4547	256.890	.2240E-05	.1245E-01	154.2	2.307	3.0E-03
-136.180	47.4497	253.005	.2567E-05	.1460E-01	157.9	2.307	2.6E-03
-135.555	47.4438	249.129	.2905E-05	.1703E-01	162.8	2.308	2.3E-03
-134.930	47.4366	245.264	.3514E-05	.1989E-01	157.2	2.308	1.9E-03
-134.305	47.4276	241.410	.4161E-05	.2330E-01	155.5	2.308	1.6E-03
-133.680	47.4167	237.565	.4911E-05	.2733E-01	154.5	2.308	1.4E-03
-133.055	47.4039	233.731	.5670E-05	.3200E-01	156.8	2.308	1.2E-03
-132.430	47.3887	229.908	.6590E-05	.3741E-01	157.6	2.308	1.0E-03
-131.805	47.3709	226.096	.7682E-05	.4367E-01	157.9	2.308	9.0E-04
-131.180	47.3497	222.295	.9075E-05	.5103E-01	156.2	2.308	7.7E-04
-130.555	47.3249	218.505	.1042E-04	.5954E-01	158.8	2.309	6.7E-04
-129.930	47.2961	214.727	.1214E-04	.6937E-01	158.8	2.309	5.8E-04
-129.305	47.2623	210.960	.1417E-04	.8082E-01	158.4	2.309	1.6E-02
-128.680	47.2231	207.206	.1627E-04	.9399E-01	160.5	2.309	1.4E-02
-128.055	47.1780	203.465	.1886E-04	.1091E+00	160.7	2.309	1.2E-02
-127.430	47.1234	199.738	.2311E-04	.1273E+00	153.0	2.309	9.9E-03
-126.805	47.0599	196.024	.2597E-04	.1483E+00	158.7	2.309	8.9E-03
-126.180	46.9895	192.325	.2909E-04	.1716E+00	163.9	2.309	8.0E-03
-125.555	46.9055	188.641	.3556E-04	.1994E+00	155.8	2.309	6.6E-03
-124.930	46.8091	184.974	.3971E-04	.2311E+00	161.7	2.309	5.9E-03
-124.305	46.6996	181.323	.4601E-04	.2671E+00	161.3	2.309	5.1E-03
-123.680	46.5692	177.692	.5525E-04	.3099E+00	155.8	2.309	4.3E-03
-123.055	46.4206	174.080	.6154E-04	.3586E+00	161.9	2.309	3.9E-03
-122.430	46.2539	170.489	.6987E-04	.4132E+00	164.3	2.309	3.4E-03
-121.805	46.0668	166.921	.7863E-04	.4744E+00	167.6	2.309	3.1E-03
-121.180	45.8582	163.376	.8858E-04	.5427E+00	170.2	2.309	2.7E-03
-120.555	45.6210	159.858	.1025E-03	.6205E+00	168.1	2.309	2.4E-03
-119.930	45.3508	156.367	.1174E-03	.7094E+00	167.9	2.309	2.1E-03
-119.305	45.0485	152.907	.1330E-03	.8090E+00	169.0	2.309	1.9E-03
-118.680	44.6959	149.479	.1598E-03	.9257E+00	160.9	2.309	1.6E-03
-118.055	44.2941	146.088	.1804E-03	.1059E+01	163.2	2.309	1.4E-03
-117.430	43.8497	142.737	.2037E-03	.1207E+01	164.7	2.309	1.3E-03
-116.805	43.3447	139.429	.2392E-03	.1377E+01	160.0	2.309	1.1E-03
-116.180	42.7651	136.170	.2787E-03	.1573E+01	156.8	2.309	9.9E-04

-115.555	42.1183	132.963	.3147E-03	.1793E+01	158.3	2.309	9.0E-04
-114.930	41.4055	129.814	.3575E-03	.2037E+01	158.4	2.309	8.2E-04
-114.305	40.6130	126.727	.4120E-03	.2312E+01	155.9	2.309	7.3E-04
-113.680	39.7216	123.709	.4807E-03	.2624E+01	151.7	2.309	6.5E-04
-113.055	38.7333	120.767	.5502E-03	.2975E+01	150.2	2.309	5.9E-04
-112.430	37.6451	117.907	.6325E-03	.3367E+01	147.9	2.309	5.4E-04
-111.805	36.4716	115.135	.7085E-03	.3798E+01	149.0	2.309	5.1E-04
-111.180	35.2275	112.457	.7896E-03	.4263E+01	150.0	2.309	4.8E-04
-110.555	33.9362	109.876	.8625E-03	.4757E+01	153.3	2.309	4.7E-04
-109.930	32.6047	107.395	.9523E-03	.5278E+01	154.0	2.309	4.5E-04
-109.305	31.2263	105.016	.1058E-02	.5834E+01	153.2	2.309	4.4E-04
-108.680	29.8277	102.741	.1146E-02	.6415E+01	155.6	2.309	4.4E-04
-108.055	28.4333	100.570	.1236E-02	.7014E+01	157.7	2.309	4.4E-04
-107.430	27.0537	98.502	.1332E-02	.7630E+01	159.2	2.309	4.5E-04
-106.805	25.6982	96.535	.1431E-02	.8260E+01	160.4	2.309	4.6E-04
-106.180	24.3787	94.665	.1532E-02	.8902E+01	161.4	2.309	4.7E-04
-105.555	23.0822	92.891	.1676E-02	.9563E+01	158.5	2.309	4.8E-04
-104.930	21.8222	91.210	.1791E-02	.1024E+02	158.8	2.309	5.0E-04
-104.305	20.6130	89.617	.1917E-02	.1092E+02	158.4	2.309	5.2E-04
-103.680	19.4497	88.110	.2066E-02	.1162E+02	156.3	2.309	5.4E-04
-103.055	18.3324	86.685	.2219E-02	.1233E+02	154.4	2.309	5.6E-04
-102.430	17.2673	85.338	.2366E-02	.1305E+02	153.2	2.309	5.9E-04
-101.805	16.2695	84.063	.2478E-02	.1376E+02	154.3	2.309	6.3E-04
-101.180	15.3216	82.858	.2681E-02	.1448E+02	150.1	2.309	6.6E-04
-100.555	14.4246	81.718	.2833E-02	.1521E+02	149.2	2.309	7.0E-04
-99.930	13.5745	80.638	.3048E-02	.1595E+02	145.4	2.309	7.4E-04
-99.305	12.7688	79.617	.3246E-02	.1669E+02	142.9	2.309	7.8E-04
-98.680	12.0135	78.650	.3421E-02	.1744E+02	141.7	2.309	8.4E-04
-98.055	11.3106	77.734	.3588E-02	.1819E+02	140.8	2.309	9.0E-04
-97.430	10.6513	76.865	.3819E-02	.1893E+02	137.7	2.309	9.5E-04
-96.805	10.0282	76.039	.4062E-02	.1969E+02	134.7	2.309	1.0E-03
-96.180	9.4429	75.255	.4266E-02	.2045E+02	133.2	2.309	1.1E-03
-95.555	8.8987	74.510	.4430E-02	.2120E+02	133.0	2.309	1.2E-03

Table III: Measurements characteristics of the Galileo ASI profile used in this paper

Altitude range, z (km)	290 - 90
Pressure range, p (mbar)	0.003-10.77
Time range, t (s from start of descent mode)	(–142)-(–104)
Latitude, (°)	6.5
West longitude, system III, (°)	4° - 3°
Number of data points per accelerometer	60
Vertical resolution (for one accelerometer), km	3.9-1.6
Vertical velocity, v_z (km/s)	6.4-2.5
Velocity, V (km/s)	47.5-20.9
Angle of attack (°)	7.7 - 6.9

Table IV: Physical characteristics of the Galileo ASI profile used in this paper

Mean gravitational acceleration, g (m s^{-2})	23.15
Mean temperature, T_0 (K)	158.1
Mean scale height, H (km)	24.6
Adiabatic lapse rate, Γ (K km^{-1})	2.11
Brunt-Väisällä frequency, N (s^{-1})	0.0174
Coriolis frequency, f (s^{-1})	4.0×10^{-5}
RMS temperature, σ_T (K)	5.0
Thermal gradients	
Mean gradient (K/km)	-0.029±0.006
Variance (K^2/km^2)	0.98±0.01
Skewness (unitless)	0.42±0.25
Power spectra	
Amplitude a (unitless)	1/10
Critical wavelength L_* (km)	30.3
Small wavelength exponent t	3
Large wavelength exponent s	0

Table V: Prominent wavetrains in Jupiter's stratosphere

	A	B	C
range in fit (km)	75-175	175-205	240-280
background temperature, b (K)	152.85±0.28	158.85±0.36	154.56±0.34
background gradient, d (K/km)	0.472±0.063	-0.153±0.042	-0.104±0.027
background 2nd derivative, q (K/km^2)	-0.0048±0.0013	0 (fixed)	0 (fixed)
wave amplitude at z_0, a (K)	-10.54±0.97	3.87±0.40	6.31±0.42
altitude of wave phase=0, z_0 (km)	108.60±0.31	190.67±0.17	267.32±0.22
vertical wavelength, $L_z = 2\pi/m$ (km)	67.93 ±3.38	10.37±0.21	23.84±0.45
damping parameter, α (1/km)	0.0223±0.0019	0.0018±0.0117	-0.0178±0.0069
diffusion timescale τ (s^{-1})	4×10^{-6}	2×10^{-4}	4×10^{-5}
wavelengths in fitted range	1.5	2.9	1.7
suggested interpretation	long-lived feature	critically damped gravity wave	undamped gravity wave